Supplementary Information

Performance of the nanopost single-photon source: beyond the single-mode model

Martin Arentoft Jacobsen,[a] Yujing Wang,[a] Luca Vannucci,[a] Julien Claudon[b], Jean-Michel Gérard,[b] and Niels Gregersen[a]

1 Height adjustment procedure

In principle, the dipole position h_t and h_b would also be free parameters if we wanted to perform a complete optimization of the nanocavity. However, this would be a very demanding task. Instead, we have chosen to study cavities with 3 antinodes as our test simulations have shown that the 2nd antinode in a 3 antinode cavity provides a good performance. Thus h_t and h_b will be fixed to ensure a cavity with 3 antinodes and a resonance wavelength of $\lambda_r = 930$nm at the 2nd antinode. A procedure is required such that h_t and h_b satisfies these conditions. The first step is to use the SMM (phase conditions of the fundamental mode) to determine the initial total height h:

$$h = (2\pi - \arg(r_{\text{bot},11}))/(2\beta_1) + (2\pi - \arg(r_{\text{top},11}))/(2\beta_1). \quad (1)$$

This is under the conditions $\arg(r_{\text{bot},11}) < 0$ and $\arg(r_{\text{top},11}) > 0$. Then we place the dipole in the second antinode from the bottom:

$$h_b = (2\pi - \arg(r_{\text{bot},11}))/(2\beta_1) \quad (2)$$

and

$$h_t = (2\pi - \arg(r_{\text{top},11}))/(2\beta_1). \quad (3)$$

However, due to the background continuum and mode-coupling, this method does not ensure that the dipole is placed exactly at an antinode nor that the resonant wavelength of the cavity corresponds exactly to the design wavelength, $(\frac{dF_P}{d\lambda})_{\lambda=\lambda_d} = 0$. To solve this problem, the dipole is first adjusted to the exact position of the antinode by plotting $|E_r(z)|^2$ and locating the peak. Then the height is slightly adjusted $h = h \pm \delta h$, while the dipole is moved to the exact position of the antinode for each adjustment until $(\frac{dF_P}{d\lambda})_{\lambda=\lambda_d} = 0$ is satisfied. Finally, the position of the 1st antinode (from the bottom) can also be identified by plotting $|E_r(z)|^2$.

Finally, we will provide the total height, h_{total} of the structure along with the height deviation between the initial height obtained from the SMM and the final height, $h_{\text{diff}} = h_{\text{total}} - h_{\text{initial}}$.
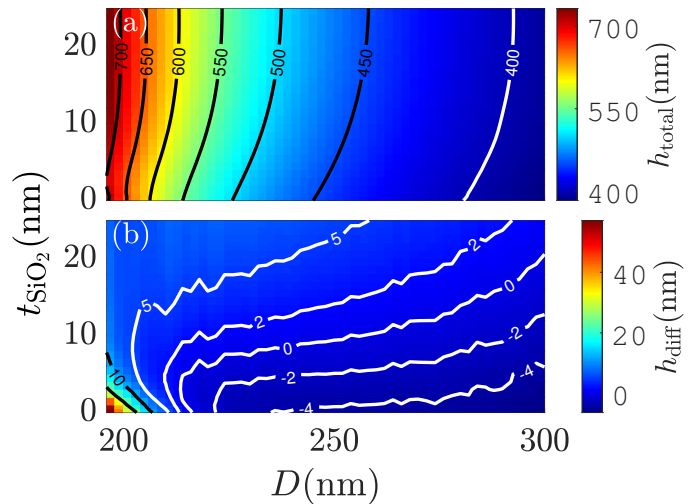
[a] DTU Electro, Department of Electrical and Photonics Engineering, Technical University of Denmark, DK-2800 Kongens Lyngby, Denmark.
[b] Univ. Grenoble Alpes, CEA, Grenoble INP, IRIG, PHELIQS, "Nanophysique et Semiconducteurs" Group, F-38000 Grenoble, France.

Fig. 1 (a) Total height of the structure, h_{total}, as a function of the diameter, D, and the silica layer thickness, t_{SiO_2}. (b) The height difference between the initial height and the final height, h_{diff}, as a function of the diameter, D, and the silica layer thickness, t_{SiO_2}.

In Fig. (1a), the total height of the structure is shown as a function of the diameter and the silica layer thickness. The total height mostly depends on the diameter as the diameter determines the propagation constant β_1 and thus the primary influence of the phase. In Fig. (1b), the height difference of the final total height compared to the SMM is shown. For most of the parameters, the difference is small in the range -5nm to 5nm. However, for the small diameters and thin silica layer thicknesses, there is a very large difference up to 50nm. This is the same parameter region where the modal reflection at the bottom interface is small. Thus the phase of the fundamental mode is less dominating compared to the contributions of the radiation and evanescent modes. Oscillations can also be observed in the height difference due to numerical noise. The exact resonance wavelength is sensitive to the height of the structure, but these oscillations are on the scale of less than 1nm, and the uncertainty in the resonance wavelength will be on a similar scale.

2 Influence of the numerical aperture

In all the simulations of the efficiency a numerical aperture of $NA = 0.75$ has been used. Here we will investigate the influence of varying the numerical aperture.
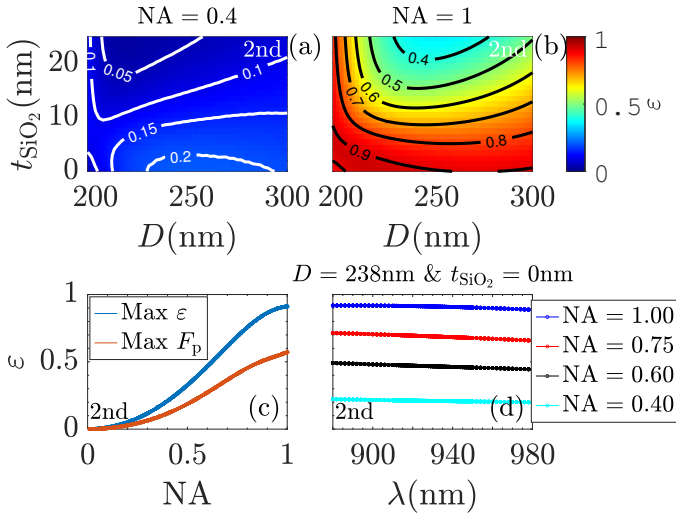
Fig. 2 Efficiency, ε, at the 2nd antinode for a numerical aperture of NA = 0.4 (a) and NA = 1.00 (b). (c) Efficiency, ε, as a function of the numerical aperture, NA, for three different parameters at the 2nd antinode. (d) Efficiency, ε, as a function of wavelength, λ, for four different values of the NA.

In Fig.(2a) and Fig.(2b) the efficiency is shown as a function of the diameter and the silica layer thickness similar to the Main Text Fig. (3a), but for a numerical aperture NA = 0.4 and NA = 1. Lowering the numerical aperture to NA = 0.4 drastically reduces the efficiency and the maximum is barely above $\varepsilon = 0.2$. This shows that a large numerical aperture is crucial for the good performance of the nanopost. By increasing the numerical aperture from NA = 0.75 ($\theta \approx 49°$) to NA = 1.00 ($\theta = 90°$) there is roughly a 20% increase in the efficiency, so there is still some light lost at angles above $\theta \approx 49°$. Furthermore, for a numerical aperture of NA = 1, the efficiency directly represents the losses to the bottom mirror. For diameters above $D = 210$ nm, an increased silica layer thickness increases the losses to the bottom mirror even though the Purcell factor increases. In Fig. (2c) the efficiency for the structures with the largest efficiency and Purcell factor, at the 2nd antinode, are shown as a function of the numerical aperture. The steepest part of the curves is roughly in the interval NA = 0.4 to NA = 0.75, which is the reason for the huge difference in efficiency between NA = 0.4 and NA = 0.75. The curves also start to flatten out as the NA reaches 1. In Fig. (2d) the efficiency is plotted for four different values of the numerical aperture as a function of the wavelength. The numerical aperture does not influence the curvature of the efficiency as a function of the wavelength. This means that being on resonance does not focus the far-field compared to being off resonance.

3 Gaussian collection efficiency

So far the efficiency has been evaluated by calculating the total power collected in the lens with some numerical aperture. However, in many applications the light will couple to a fiber afterwards. Therefore we have also calculated the power overlap between the emitted far-field and the far-field of a Gaussian representative for the fundamental mode in many single-mode fibers[1]. The applied method is identical to the one presented in
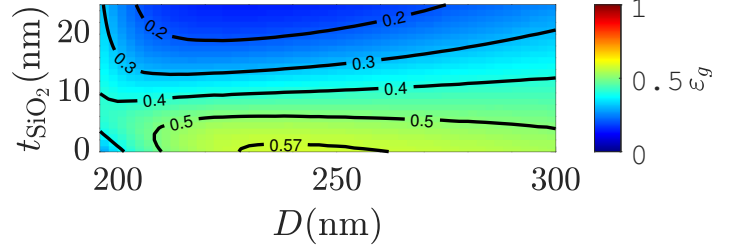

Fig. 3 Gaussian collection efficiency, ε_g, as a function of the diameter, D, and the silica layer thickness, t_{SiO_2}, for the 2nd antinode. NA = 0.75.

the appendix of[2], and the Gaussian collection efficiency is defined as $\varepsilon_g = P_{\text{collected,Gaussian}}/P_T$, where $P_{\text{collected,Gaussian}}$ is defined as the overlap with a Gaussian profile. In Fig. (3) the Gaussian efficiency is shown for the 2nd antinode. Compared to the standard efficiency in the Main Text Fig. (3a), the difference is approximately 0.1 over the entire parameter space, showcasing the Gaussian shaped profile of the far-field.

4 Efficiency analysis for the structure with maximum Purcell factor

We will now apply the efficiency analysis for the structure with the largest Purcell factor with the parameters $D = 250$ nm and $t_{SiO_2} = 13$ nm and an efficiency of $\varepsilon = 0.41$.

In Fig. (4) the efficiency is shown as a function of the initial coefficients (Fig. (4a)) and the final coefficients (Fig. (4b)), expressed with the propagation constant $(\beta/k_0)^2$, just as for the structure with maximum efficiency. Again the curve in Fig. (4a) is flat and the channels of the fundamental mode dominates the efficiency. The efficiency increase by adding the final coefficients, i.e. c_2 and c_3, seen in Fig. (4b), is still significant, but much smaller compared to the structure with maximum efficiency. Here the increase is from approximately $\varepsilon = 0.3$ to $\varepsilon = 0.41$. The curve in Fig. (4b) also flattens out completely due to the numerical aperture.
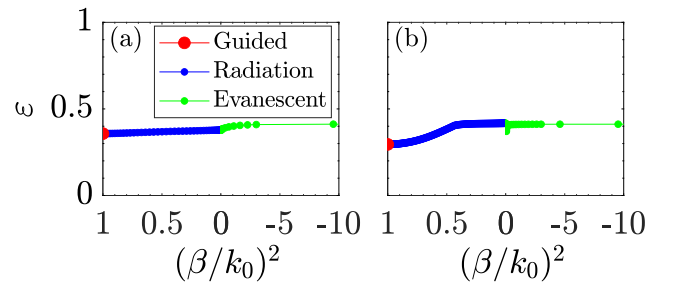

Fig. 4 (a) Efficiency, ε (NA = 0.75), as a function of the initial coefficients expressed with the propagation constant $(\beta/k_0)^2$. (b) Efficiency, ε (NA = 75), as a function of the final coefficients expressed with the propagation constant $(\beta/k_0)^2$.
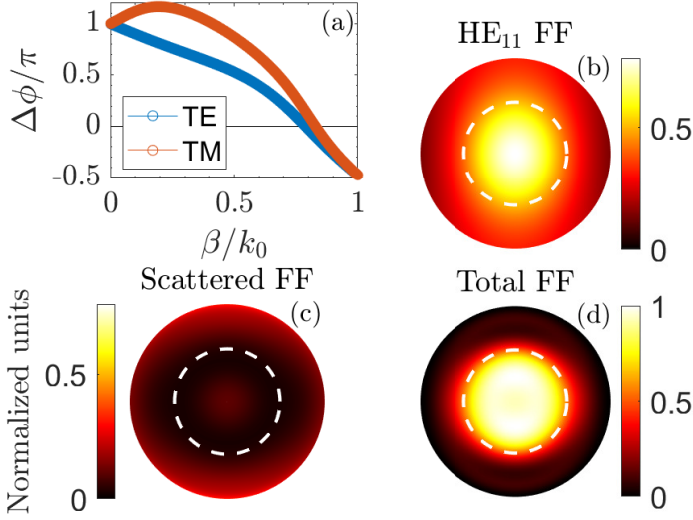
Fig. 5 (a) The phase difference between the direct transmission of the fundamental mode and the background continuum for TE and TM modes as a function of the propagation constant. (b) The far-field of the fundamental mode. (c) The far-field of the background continuum. (d) The total far-field. The white dotted line indicates $NA = 0.75$. Be aware of the different color scales that have been used for the far-fields.

In Fig. (5a) the phase difference in the air layer between the direct transmission of the fundamental mode and the entire background is shown as a function of the propagation constant for TE and TM modes. We observe similar features as before, i.e. constructive (destructive) interference for light propagating vertically (horizontally). Though at $\beta/k_0 = 1$, the phase difference is larger compared to the previous structure. In Fig. (5b), Fig. (5c) and Fig. (5d) the far-fields of the direction transmission of the fundamental mode, the background radiation and the total field is shown. Compared to the structure with maximum efficiency, the far-field of the background radiation is significantly different. Here, the far-field is mainly focused towards horizontal angles and the intensity is much smaller compared to the far-field of HE_{11}. As such the constructive contribution at smaller angles is not as significant and less of the radiation will be captured by the lens, due to the numerical aperture. This explains why the efficiency increase in Fig. (4b) is much smaller compared the structure with the maximum efficiency. However, there is still destructive interference for the light that propagates horizontally. As such the interference between the direction emission and the radiation focuses the far-field, but not to the same degree as for the structure with the maximum efficiency.

5 Purcell factor analysis for the structure with maximum collection efficiency

We will now apply the model for the Purcell factor for the structure with the largest efficiency, $D = 238\,\mathrm{nm}$ and $t_{SiO_2} = 0\,\mathrm{nm}$ and $F_p = 4.8$.

In Fig. (6) the Purcell factor is shown as a function of the dipole position throughout the cavity, both the full model (n. 7) and the SMM (n. 1) are used. Here the 3 antinodes can be observed and the SMM predicts a larger Purcell factor for all 3 antinodes
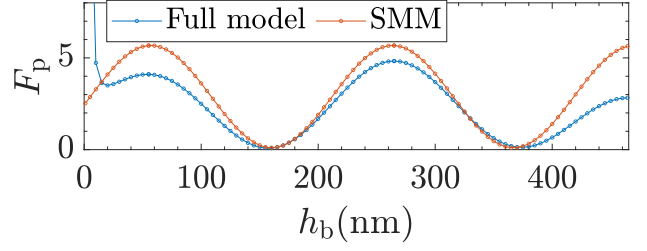

Fig. 6 Purcell factor, F_p, computed using the full model and the SMM as a function of the dipole position from the bottom interface, h_b. $D = 238\,\mathrm{nm}$ and $t_{SiO_2} = 0\,\mathrm{nm}$.

compared to the full model. The positions of the antinodes are almost identical between the full model and the SMM. The Purcell factor increases drastically when the dipole is placed close to the metal mirror due to non-radiative decay processes[3].
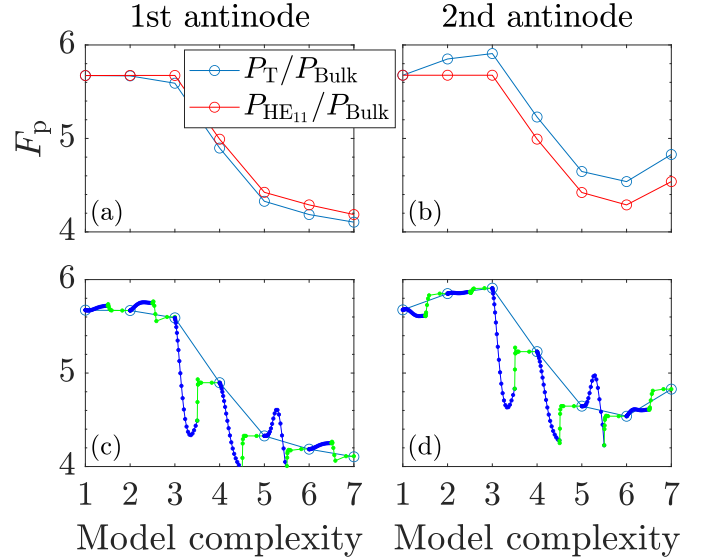

Fig. 7 Purcell factor (P_T/P_{Bulk}) and fundamental mode enhancement ($P_{HE_{11}}/P_{Bulk}$) for the 1st (a) and 2nd (b) antinode as a function of the model number. In (c) and (d) the background continuum is continuously included between each model number.

In Fig. (7a) and Fig. (7b) the Purcell factor and the power enhancement of the fundamental mode is shown as a function of the model complexity for the 1st and 2nd antinode. Compared to the structure with $D = 250\,\mathrm{nm}$ and $t_{SiO_2} = 13\,\mathrm{nm}$, there are a few differences. The SMM predicts a smaller Purcell factor, which is simply caused by the lower modal reflection at the bottom. There is a large negative contribution when including the back-scattering at the bottom interface (n 5.) at both antinodes. This is caused by the change of the silica layer thickness and as seen in Fig. (7c) and Fig. (7d). The propagating radiation modes are responsible for this decrease. Furthermore, by including the scattering of the background to itself (n. 6), there is now a small decrease for both antinodes. These are the differences between the two structures. The differences between the 1st and 2nd antinode are exactly the same for the two structures, where the scattering into evanescent

modes at the top interface (n. 2) and the initial evanescent modes provide a positive contribution at the 2nd antinode.

6 Asymmetric wavelength dependence for the two antinodes

To further study the resonance shift between the 1st and 2nd antinodes, we choose a nanopost design of $D = 202\,\text{nm}$ and $t_{\text{SiO}_2} = 5\,\text{nm}$, where the shift is more pronounced.
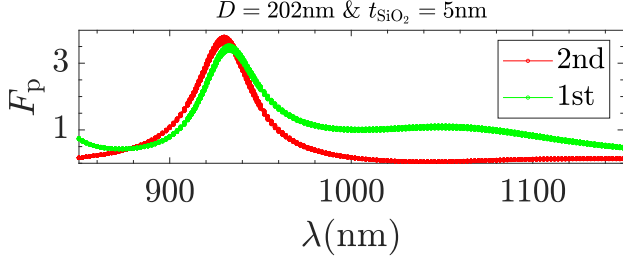

Fig. 8 Purcell factor, F_p, as a function of wavelength, λ, for the two antinodes. The parameters are $D = 202\,\text{nm}$ and $t_{\text{SiO}_2} = 5\,\text{nm}$.

In Fig. (8) the Purcell factor is shown for the two antinodes as a function of the wavelength. The peak positions of the Purcell factors (resonance wavelength) are $\lambda_{2nd,r} = 930\,\text{nm}$ and $\lambda_{1st,r} = 933\,\text{nm}$. By observing the curve for the 1st antinode, this shift is caused by another broad resonance at approximately $\lambda = 1050\,\text{nm}$. To gain further insight into the resonances of the structure and verify our results, we have performed a quasi-normal mode (QNM) simulation[4] of the nanopost. In this simulation 15 QNMs are found and the complex eigenfrequencies, $\tilde{\omega}_\mu = \omega_\mu - i\gamma_\mu$, of the 3 important QNMs are $\tilde{\omega}_{\text{QNM}_1} = 2.0237 \times 10^{15} - i4.4904 \times 10^{13}\,\text{Hz}$, $\tilde{\omega}_{\text{QNM}_2} = 1.7595 \times 10^{15} - i1.4654 \times 10^{14}\,\text{Hz}$ and $\tilde{\omega}_{\text{QNM}_3} = 2.2809 \times 10^{15} - i2.0703 \times 10^{13}\,\text{Hz}$. The corresponding real parts of the complex wavelength are $\lambda_{\text{QNM}_1} = 930.3\,\text{nm}$, $\lambda_{\text{QNM}_2} = 1063.2\,\text{nm}$ and $\lambda_{\text{QNM}_3} = 825.8\,\text{nm}$. The Q factors of the QNMs can also be calculated using $Q_\mu = \omega_\mu/(2\gamma_\mu)$[4], and we obtain $Q_{\text{QNM}_1} = 22.5$, $Q_{\text{QNM}_2} = 6.0$ and $Q_{\text{QNM}_3} = 55.1$.

In Fig. (9a,9b), the comparison of the Purcell factor between the FMM and the QNM simulation is shown for the two antinodes. Overall, the quantitative agreement between the FMM and QNM simulations is good with some small deviations. In Fig. (9a), the individual contributions of 3 QNMs are plotted along with their sum and the result of the FMM for the 1st antinode. These 3 QNMs provide a good description of the overall Purcell factor and they directly correspond to the peaks in the spectrum. QNM_1 and QNM_2 also overlap in the spectrum due to the low Q factor of QNM_2, which slightly shifts the peak position of the total Purcell factor. In Fig. (9b), the individual contributions of 2 QNMs are plotted along with their sum and the result of the FMM for the 2nd antinode. Here QNM_1 is almost sufficient to describe the entire spectrum, and we do not observe any other peaks than the one at $\lambda = 930\,\text{nm}$, besides a small bump at longer wavelengths. Now, consider the in-plane electrical field profiles of the 3 QNMs shown in Fig. (9c,9d,9e). QNM_1 has 3 antinodes, QNM_2 has 2 antinodes and QNM_3 has 4 antinodes. The green star corresponds to the position of the 1st antinode, where the QD is
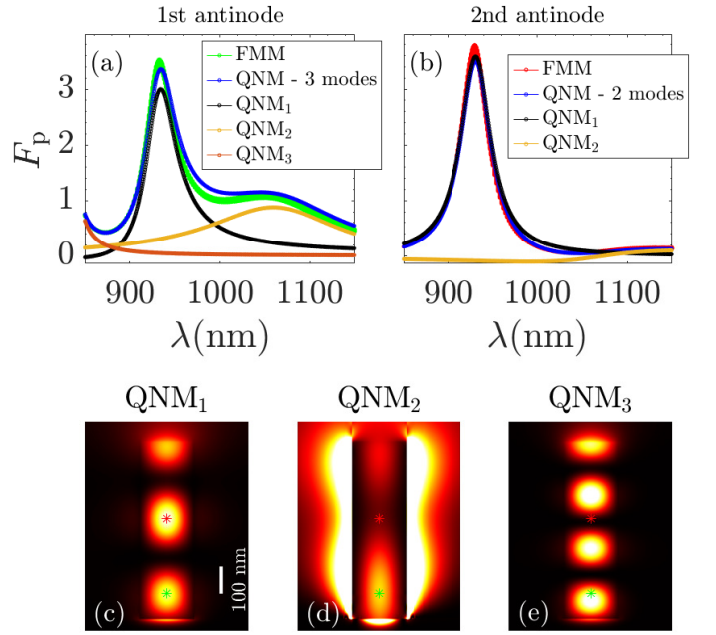

Fig. 9 Comparison of the Purcell factor between the FMM and the QNM simulation for the 1st antinode (a) and the 2nd antinode (b). In-plane electrical field profiles of the 3 QNMs at their resonance wavelengths are shown in (c), (d) and (e). The green star corresponds to the position of the 1st antinode, and the red star corresponds to the position of the 2nd antinode. The white scale bar in (a) corresponds to 100 nm. The intensity is scaled in each field plot and should not be used for comparison.

placed, and this position is very close to an antinode for QNM_2 and QNM_3. Therefore the contributions of these QNMs appear in the spectrum. However, the position of the 2nd antinode (red star) is much closer to a node for QNM_2 and QNM_3, and therefore they do not influence the spectrum.

References

1 M. Munsch, N. S. Malik, E. Dupuy, A. Delga, J. Bleuse, J.-M. Gérard, J. Claudon, N. Gregersen and J. Mørk, *Phys. Rev. Lett.*, 2013, **110**, 177402.

2 B.-Y. Wang, E. V. Denning, U. M. Gür, C.-Y. Lu and N. Gregersen, *Phys. Rev. B*, 2020, **102**, 125301.

3 L. Novotny and B. Hecht, *Principles of Nano-Optics*, Cambridge University Press, 2012.

4 J. R. de Lasson, P. T. Kristensen, J. Mørk and N. Gregersen, *Opt. Lett.*, 2015, **40**, 5790–5793.